


Polaronic transport and thermoelectricity in $\text{Fe}_{1-x}\text{Co}_x\text{Sb}_2\text{S}_4$ ($x = 0, 0.1, \text{ and } 0.2$)Yu Liu (刘育),¹ Chang-Jong Kang,² Eli Stavitski,³ Qianheng Du (杜乾衡),^{1,4}
Klaus Attenkofer,³ G. Kotliar,^{1,2} and C. Petrovic^{1,4}¹*Condensed Matter Physics and Materials Science Department, Brookhaven National Laboratory, Upton, New York 11973, USA*²*Department of Physics and Astronomy, Rutgers University, Piscataway, New Jersey 08856, USA*³*National Synchrotron Light Source II, Brookhaven National Laboratory, Upton, New York 11973, USA*⁴*Department of Materials Science and Chemical Engineering, Stony Brook University, Stony Brook, New York 11790, USA* (Received 17 November 2017; published 9 April 2018; corrected 14 January 2020)

We report a study of Co-doped berthierite $\text{Fe}_{1-x}\text{Co}_x\text{Sb}_2\text{S}_4$ ($x = 0, 0.1, \text{ and } 0.2$). The alloy series of $\text{Fe}_{1-x}\text{Co}_x\text{Sb}_2\text{S}_4$ crystallize in an orthorhombic structure with the $Pnma$ space group, similar to FeSb_2 , and show semiconducting behavior. The large discrepancy between activation energy for conductivity, E_ρ (146 ~ 270 meV), and thermopower, E_S (47 ~ 108 meV), indicates the polaronic transport mechanism. Bulk magnetization and heat-capacity measurements of pure FeSb_2S_4 ($x = 0$) exhibit a broad antiferromagnetic transition ($T_N = 46$ K) followed by an additional weak transition ($T^* = 50$ K). Transition temperatures (T_N and T^*) slightly decrease with increasing Co content x . This is also reflected in the thermal conductivity measurement, indicating strong spin-lattice coupling. $\text{Fe}_{1-x}\text{Co}_x\text{Sb}_2\text{S}_4$ shows relatively high value of thermopower (up to $\sim 624 \mu\text{V K}^{-1}$ at 300 K) and thermal conductivity much lower when compared to FeSb_2 , a feature desired for potential applications based on FeSb_2 materials.

DOI: [10.1103/PhysRevB.97.155202](https://doi.org/10.1103/PhysRevB.97.155202)**I. INTRODUCTION**

Correlated electron materials may enable transformative changes in thermoelectric energy creation and conversion. The Kondo-insulator-like semiconductor FeSb_2 features not only strong electronic correlations but also the highest thermoelectric power factor in nature and thermopower up to 45 mV K^{-1} [1–6]. For predictive theory modeling of correlated electron thermoelectricity, a similar chemically tunable material is of high interest.

The ternary MPn_2Q_4 ($M = \text{Mn, Fe; Pn} = \text{Sb, Bi; Q} = \text{S, Se}$) compounds are typically magnetic semiconductors that exhibit high thermopower and rather tunable electronic, magnetic, and thermoelectric properties [7–21]. For instance, antiferromagnetic (AFM) ordering can be observed in FeSb_2S_4 [16–19], MnSb_2S_4 [7–10], MnSb_2Se_4 [11–13], and MnBi_2Se_4 [14,15], whereas FeSb_2Se_4 and FeBi_2Se_4 exhibit ferromagnetic (FM) behavior [20,21]. Moreover, p -type semiconducting behavior is observed in MnSb_2Se_4 and FeSb_2Se_4 with a semiconductor-to-insulator transition for FeSb_2Se_4 below 130 K [11–13,20], but MnBi_2Se_4 and FeBi_2Se_4 are n -type semiconductors [14,15,21].

Among these compounds, FeSb_2S_4 shows a helicoidal-type AFM order below $T_N = 50$ K with Fe^{2+} moments parallel to the ab plane and a noncommensurate propagation vector along the c axis [18]. The unit cell contains four FeSb_2S_4 , in which Fe atoms are surrounded by six S atoms in a distorted octahedral arrangement. The FeS_6 octahedra share edges to form chains parallel to the b axis [Fig. 1(a)], which is similar to FeSb_2 [22–24]. The chains are connected together via S-Sb-S bonds with some rather short Sb-S distances (2.43 Å and 2.48 Å), suggesting strong covalence of these bonds, whereas the large Fe-S distances (2.45 ~ 2.62 Å) indicate that the Fe-S bond is rather ionic and that Fe is in the $3d_6$

high-spin Fe^{2+} state [16,18]. Furthermore, FeSb_2S_4 features a lone Sb^{3+} pair, which could increase anharmonicity of bonds and enhance phonon-phonon scattering [19]. In contrast to literature devoted to MnPn_2Q_4 or FeSb_2Se_4 , there are no studies of FeSb_2S_4 thermoelectric and/or physical properties tuning yet. The evolution of crystal structure tuned by 50% Bi or Nd doped at Sb site was studied without physical properties measurements [25,26].

Here, we investigate a series of Co-doped berthierite $\text{Fe}_{1-x}\text{Co}_x\text{Sb}_2\text{S}_4$ ($x = 0, 0.1, \text{ and } 0.2$). In contrast to $\text{Fe}_{1-x}\text{Co}_x\text{Sb}_2$ and $\text{Fe}_{1-x}\text{Cr}_x\text{Sb}_2$, where electronic transport is dominated by thermal activation and variable range hopping (VRH) [27,28], our results indicate polaronic transport and strong spin-lattice coupling. Higher ionicity of chemical bonds in Fe-S octahedra when compared to Fe-Sb octahedra inhibits electrical conductivity. In contrast to FeSb_2 , however, in these materials we report lower thermal conductivity when compared to FeSb_2 due to induced phonon-scattering lattice distortions and disorder introduced by Co atoms.

II. EXPERIMENTAL DETAILS

$\text{Fe}_{1-x}\text{Co}_x\text{Sb}_2\text{S}_4$ polycrystals were synthesized via solid-state reaction starting from an intimate mixture of high-purity elements: Fe powder (99.99%, Alfa Aesar), Co powder (99.99%, Alfa Aesar), Sb pieces (99.999%, Alfa Aesar), and S powder (99.9%, Alfa Aesar) with a molar ratio of $1 - x : x : 2 : 4$. The starting materials were mixed and ground in an agate mortar, then pressed into pellets and sealed in an evacuated quartz tube backfilled with pure argon gas. The tube was heated to 300 °C over 10 h, held at 300 °C for 10 h, and then slowly heated to 500 °C and reacted for 5 d followed by furnace cooling. This procedure was repeated several times to ensure homogeneity. Powder x-ray diffraction (XRD) data were taken

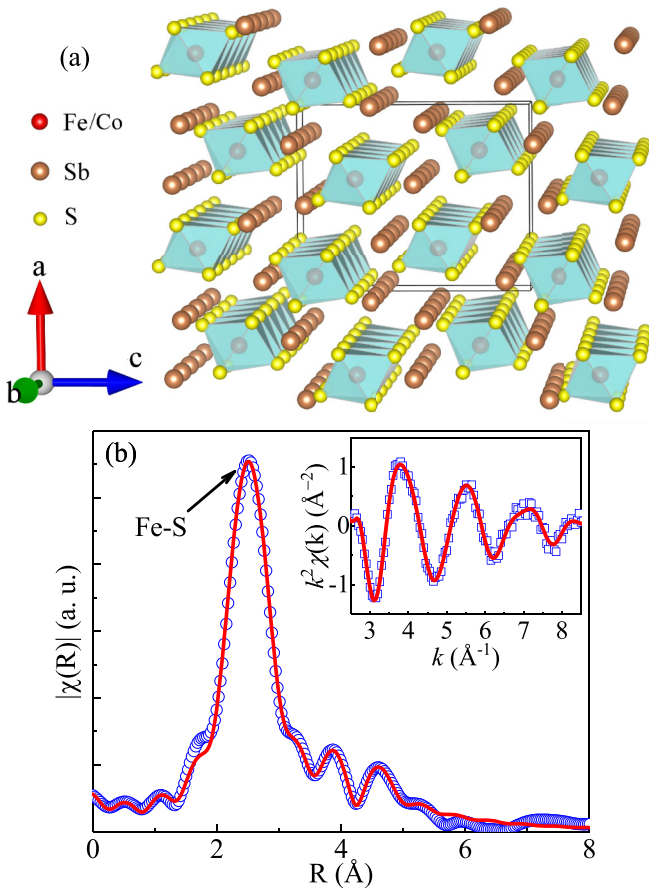


FIG. 1. (a) Crystal structure. (b) Fourier-transform magnitudes of the extended x-ray absorption fine structure (EXAFS) data of FeSb_2S_4 measured at room temperature. The experimental data are shown as blue symbols alongside the model fit plotted as a red line. Inset in (b) shows the corresponding EXAFS oscillation with the model fit.

with $\text{Cu K}\alpha$ ($\lambda = 0.15418$ nm) radiation of a Rigaku Miniflex powder diffractometer. The structural parameters were obtained by Rietveld refinement using RIETICA software. X-ray absorption spectroscopy was measured at 8-ID beamline of the National Synchrotron Light Source II at Brookhaven National Laboratory in the transmission mode. The extracted extended x-ray absorption fine structure (EXAFS) signal, $\chi(k)$, was weighed by k^2 to emphasize the high-energy oscillation and then Fourier-transformed in a k range from 2.5 to 8.5 \AA^{-1} to analyze the data in R space. Thermal, transport, and magnetic measurements were carried out in the Quantum Design PPMS-9 and MPMS-5 systems. The electronic structure of the nonmagnetic FeSb_2S_4 is calculated within the full-potential linearized augmented plane-wave method implemented in the WIEN2k package [29,30]. The general gradient approximation (GGA) was used for exchange-correlation potential [31]. The Brillouin zone is sampled with a Gamma-centered $12 \times 38 \times 10$ k -space mesh.

III. RESULTS AND DISCUSSIONS

The crystal structure of FeSb_2S_4 was first determined by Buerger *et al.* [32]. The structure contains three distinct

cation positions: Fe^{2+} has an octahedral coordination and the polyhedra share edges with two conjugate Sb^{3+} coordination polyhedra [19]. The Fe^{2+} coordination octahedra also share opposite edges among themselves and form chains along [010], similar to FeSb_2 , but with Sb^{3+} cations inserted between the chains [Fig. 1(a)] [16]. The local structure was determined by EXAFS spectra [Fig. 1(b)] of FeSb_2S_4 measured at room temperature. In the single-scattering approximation, the EXAFS could be described by the following equation [33]:

$$\chi(k) = \sum_i \frac{N_i S_0^2}{k R_i^2} f_i(k, R_i) e^{-\frac{2R_i}{\lambda}} e^{-2k^2 \sigma_i^2} \sin[2k R_i + \delta_i(k)],$$

where N_i is the number of neighboring atoms at a distance R_i from the photoabsorbing atom. S_0^2 is the passive electrons reduction factor, $f_i(k, R_i)$ is the backscattering amplitude, λ is the photoelectron mean free path, δ_i is the phase shift, and σ_i^2 is the correlated Debye-Waller factor measuring the mean-square relative displacement of the photoabsorber-backscatter pairs. In FeSb_2S_4 , the first nearest neighbors of Fe atoms are six S atoms located at $2.45 \text{ \AA} \sim 2.62 \text{ \AA}$, and the second-nearest neighbors are Fe atoms and Sb atoms at about 3.76 \AA [16]. As shown in Fig. 1(b), the corrected main peak around $R \sim 2.5 \text{ \AA}$ in the Fourier-transform magnitudes of Fe K-edge EXAFS corresponds to three different Fe-S bond distances with $2.449(2) \text{ \AA}$, $2.501(2) \text{ \AA}$, and $2.614(2) \text{ \AA}$ extracted from the model fits with N fixed to 2 and $\sigma^2 = 0.014 \text{ \AA}^2$. The peaks between 3.6 \AA and 5.0 \AA are due to longer Fe-Fe ($\sim 3.765 \text{ \AA}$) and Fe-Sb ($\sim 3.762 \text{ \AA}$, 4.000 \AA , 4.316 \AA , and 4.521 \AA) bond distances, and the multiple scattering involving different near neighbours of the Fe atoms. The salient features of the local crystallographic environment of Fe atoms are in good agreement with the previous studies of the average crystal structure [32].

Figure 2(a) shows the structural refinement of powder XRD for $\text{Fe}_{1-x}\text{Co}_x\text{Sb}_2\text{S}_4$ ($x = 0, 0.1, \text{ and } 0.2$), indicating that all reflections can be well indexed in the $Pnma$ space group. A tiny peak ($\sim 35^\circ$) of CoSbS emerges as $x = 0.2$ (less than 5%), in line with the absence of a stable phase of CoSb_2S_4 . For pure

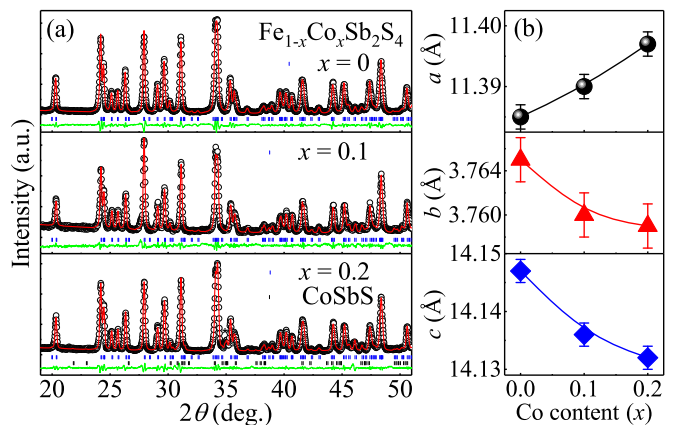


FIG. 2. (a) Powder x-ray diffraction (XRD) patterns for $\text{Fe}_{1-x}\text{Co}_x\text{Sb}_2\text{S}_4$ ($x = 0, 0.1, \text{ and } 0.2$). Impurity peak of CoSbS is labeled by an asterisk. (b) The evolution of lattice parameters a , b , and c .

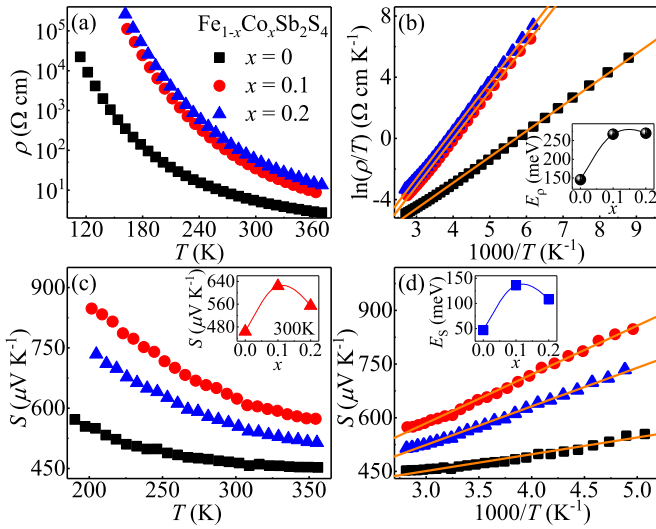


FIG. 3. (a) Temperature-dependent electrical resistivity $\rho(T)$ of $\text{Fe}_{1-x}\text{Co}_x\text{Sb}_2\text{S}_4$ ($x = 0, 0.1, \text{ and } 0.2$). (b) $\ln(\rho/T)$ vs $1000/T$ curves fitted by the adiabatic small polaron hopping model, $\rho(T) = AT\exp(E_\rho/k_B T)$, where E_ρ is activation energy and k_B is Boltzmann constant. Inset: The evolution of E_ρ . (c) Temperature-dependent thermopower $S(T)$ of $\text{Fe}_{1-x}\text{Co}_x\text{Sb}_2\text{S}_4$ ($x = 0, 0.1, \text{ and } 0.2$). Inset: the values of thermopower at room temperature. (d) $S(T)$ vs $1000/T$ curves fitted using $S(T) = (k_B/e)(\alpha + E_S/k_B T)$, where E_S is activation energy. Inset: The evolution of E_S .

FeSb_2S_4 , the determined lattice parameters $a = 11.385(2) \text{ \AA}$, $b = 3.765(2) \text{ \AA}$, and $c = 14.147(2) \text{ \AA}$, which are reasonably smaller than those of orthorhombic MnSb_2S_4 ($a = 11.459 \text{ \AA}$, $b = 3.823 \text{ \AA}$, and $c = 14.351 \text{ \AA}$) [9]. Mössbauer spectra and theoretical calculations for FeSb_2S_4 and MnSb_2S_4 suggest that Fe^{2+} and Mn^{2+} are in the high-spin state [9,18]. This is in agreement with $r_{\text{Fe}^{2+}} (0.78 \text{ \AA}) < r_{\text{Mn}^{2+}} (0.83 \text{ \AA})$ for the high-spin state with sixfold coordination. Figure 2(b) shows the evolution of lattice parameters with Co doping content x , in which the relative change of a slightly increases with x ($\delta_a \approx 0.11\%$), whereas b and c monotonously decrease with x ($\delta_b \approx -0.16\%$ and $\delta_c \approx -0.11\%$).

Temperature-dependent electrical resistivity $\rho(T)$ for $\text{Fe}_{1-x}\text{Co}_x\text{Sb}_2\text{S}_4$ ($x = 0, 0.1, \text{ and } 0.2$) is depicted in Fig. 3(a), showing an obvious semiconducting behavior. The value of room temperature resistivity (ρ_{300K}) is about 5.6 \Omega cm for FeSb_2S_4 , which is smaller than the value of 16 \Omega cm for FeSb_2Se_4 [20], and it gradually increases to 35 \Omega cm and 62 \Omega cm for $\text{Fe}_{1-x}\text{Co}_x\text{Sb}_2\text{S}_4$ with $x = 0.1$ and 0.2 , respectively. Three typical models are considered to describe the semiconducting behavior: (i) thermally activated model, $\rho(T) = \rho_0 \exp(\frac{E_\rho}{k_B T})$, where E_ρ is activation energy; (ii) adiabatic small polaron hopping model, $\rho(T) = AT \exp(\frac{E_\rho}{k_B T})$ [34]; and (iii) Mott's VRH model, $\rho(T) = \rho_0 \exp(\frac{T_0}{T})^{1/4}$. To well understand the transport mechanism in this system, it is necessary to fit the resistivity curves based on these three formulas. Figure 3(b) shows the fitting result of the adiabatic small polaron hopping model. The extracted activation energy E_ρ [inset in Fig. 3(b)] is about $146(1) \text{ meV}$ for $x = 0$, and gradually increases to $270(1) \text{ meV}$ for $x = 0.2$. For FeSb_2S_4 ,

the estimated band gap of about $0.292(2) \text{ eV}$ is relatively smaller than the values of FeSb_2Se_4 (0.33 eV) [20], MnSb_2S_4 (0.77 eV) [10], and MnSb_2Se_4 (0.31 eV) [11]. In fact, the $\rho(T)$ curves can also be well fitted using the thermally activated model but not the VRH model.

To distinguish the thermally activated model and polaron hopping model, we further measured temperature-dependent thermopower $S(T)$. The $S(T)$ shows positive values in the whole temperature range [Fig. 3(c)], indicating dominant hole-type carriers. In the inset in Fig. 3(c), the room temperature S_{300K} value of FeSb_2S_4 is about 464 \mu V K^{-1} . The Co doping at Fe site increases thermopower S and reaches $S_{300K} = 624 \text{ \mu V K}^{-1}$ for $\text{Fe}_{1-x}\text{Co}_x\text{Sb}_2\text{S}_4$ with $x = 0.1$. It gradually increases with the decreasing temperature to a value of 848 \mu V K^{-1} at 200 K . As shown in Fig. 3(d), the $S(1000/T)$ curves of all samples show similar shape and can be fitted with the equation $S(T) = \frac{k_B}{e}(\alpha + \frac{E_S}{k_B T})$ [34], where E_S is activation energy and α is a constant. The obtained activation energy for thermopower, E_S ($47 \sim 108 \text{ meV}$) [inset in Fig. 3(d)] are much smaller than those for conductivity, E_ρ ($146 \sim 270 \text{ meV}$) [inset in Fig. 3(b)]. The large discrepancy between E_S and E_ρ typically reflects the polaron transport mechanism of carriers. According to the polaron model, the E_S is the energy required to activate the hopping of carriers, while E_ρ is the sum of the energy needed for the creation of carriers and activating the hopping of carriers [34]. Therefore, within the polaron hopping model, the activation energy E_S is smaller than E_ρ .

Temperature dependence of dc magnetic susceptibility $\chi(T) = M/H$ taken in $H = 5 \text{ T}$ for $\text{Fe}_{1-x}\text{Co}_x\text{Sb}_2\text{S}_4$ with zero-field cooling (ZFC) and field cooling (FC) modes are shown in Fig. 4(a). A broad susceptibility maximum around $T \approx 50 \text{ K}$ was observed in FeSb_2S_4 , in agreement with the previous

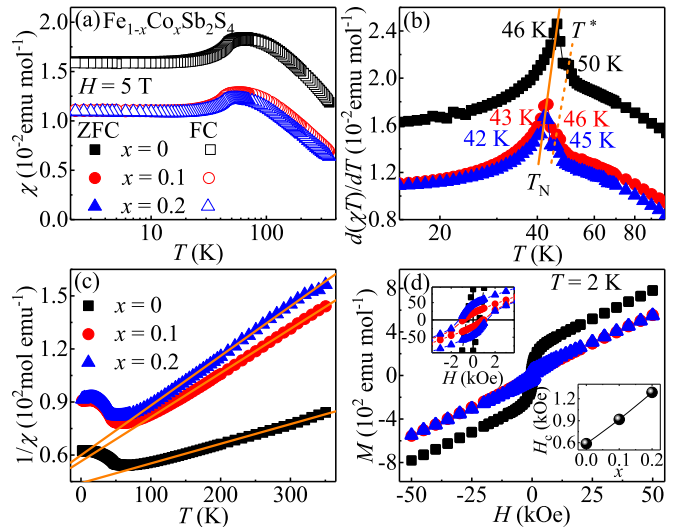


FIG. 4. (a) Temperature-dependent magnetic susceptibility obtained at $H = 5 \text{ T}$ with zero-field cooling (ZFC) and field cooling (FC) modes. (b) $1/\chi$ vs T fitted by the modified Curie-Weiss law $\chi = \chi_0 + \frac{C}{T-\theta}$, where χ_0 is the temperature-independent susceptibility, C is the Curie-Weiss constant, and θ is the Weiss temperature. (c) $d(\chi T)/dT$ vs T curves. The solid and dashed lines are guides to the eye. (d) The hysteresis loops taken at $T = 2 \text{ K}$ of $\text{Fe}_{1-x}\text{Co}_x\text{Sb}_2\text{S}_4$ ($x = 0, 0.1, \text{ and } 0.2$). Inset: The magnification in the low field region and the evolution of coercive field H_c .

report [17]. It implies that there is a low-dimensional AFM spin correlation among Fe^{2+} ions. As shown in Fig. 4(b), the AFM transition temperatures (T_N) of $\text{Fe}_{1-x}\text{Co}_x\text{Sb}_2\text{S}_4$ ($x = 0, 0.1, \text{ and } 0.2$) are defined by the maxima of $d(\chi T)/dT$ vs T curves. With Co doping, the AFM transition is robust and T_N shows weak shift to lower temperatures. Additionally, no divergence of the ZFC and FC curves was observed in $\text{Fe}_{1-x}\text{Co}_x\text{Sb}_2\text{S}_4$, which is different from the other members of MPn_2Q_4 ($M = \text{Mn, Fe; Pn} = \text{Sb, Bi; and Q} = \text{S, Se}$) system [8,11,15,20,21]. Taking into account the large intralayer distance of ~ 7 Å and the interlayer separation of ~ 15 Å between MQ_6 magnetic chains within the crystal structure of MPn_2Q_4 system, the magnetic properties are mostly controlled by the nature and magnitude of indirect exchange interactions between adjacent magnetic atoms through the bridging Q atoms within the individual MQ_6 magnetic chain (intrachain). Within the single chain of FeS_6 octahedra, according to the Goodenough-Kanamori rules [35], superexchange interactions at 90° are AFM. Furthermore, the T_N of FeSb_2S_4 (~ 46 K) is higher than that of MnSb_2S_4 (~ 25 K), implying stronger interaction due to smaller Fe-S-Fe distance [8]. It is also reflected by the evolution of T_N in Mn-based MnPn_2Q_4 , in which the T_N of MnSb_2S_4 (~ 25 K) with smaller Mn-S-Mn distance is higher than those of MnSb_2Se_4 (~ 20 K) and MnBi_2Se_4 (~ 15 K) with larger Mn-Se-Mn distances [8,11,15]. The susceptibility data above 100 K could be well fitted to the modified Curie-Weiss law, $\chi = \chi_0 + \frac{C}{T-\theta}$, where χ_0 is the temperature-independent susceptibility, C is the Curie-Weiss constant, and θ is the Weiss temperature. As shown in Fig. 4(c), a linear fit of the $1/\chi$ curve of FeSb_2S_4 yields the Weiss temperature $\theta = -397(1)$ K, confirming predominantly AFM interaction between Fe^{2+} moments. With Co doping, the value of θ changes to $-226(1)$ K and $-213(1)$ K for $\text{Fe}_{1-x}\text{Co}_x\text{Sb}_2\text{S}_4$ with $x = 0.1$ and 0.2 , respectively, indicating weakened AFM interactions. The decrease in the absolute value of $|\theta|$ is in line with the evolution of T_N [Fig. 4(c)] in $\text{Fe}_{1-x}\text{Co}_x\text{Sb}_2\text{S}_4$ ($x = 0, 0.1, \text{ and } 0.2$). Then the ratio $f = |\theta|/T_N$ could be calculated, which is about 8.63 for $x = 0$ and decreases to 5.26 for $x = 0.1$ and 5.07 for $x = 0.2$, indicating moderate spin frustration in this system [36,37]. Moreover, there is an additional weak peak T^* just above T_N in the $d(\chi T)/dT$ vs T curve, which is also confirmed by the heat-capacity measurement (see the discussion below). The two-step magnetic transition was also observed in iron-based Fe_{1+x}Te with $x \geq 0.13$ [38], benavidesite $\text{MnPb}_4\text{Sb}_6\text{S}_{14}$ [8], and manganese-based MnBiS_2Cl [39]. Whereas the FeSb_2S_4 Mössbauer experiment suggests a helicoidal-type AFM ground state with Fe^{2+} moments parallel to the ab plane and with a noncommensurate propagation vector along the c axis, neutron diffraction studies are necessary to shed more details on the two-step transition [18,40]. The hysteresis loops measured at $T = 2$ K show a weak FM component at low fields, which might be caused by spin canting and/or magnetocrystalline anisotropy, as shown in Fig. 4(d). This FM component increases with increasing x [inset of Fig. 4(d)], which is certified by the increase of coercive field H_c .

Figure 5 represents the temperature-dependent thermal conductivity $\kappa(T)$ of $\text{Fe}_{1-x}\text{Co}_x\text{Sb}_2\text{S}_4$ ($x = 0, 0.1, \text{ and } 0.2$). In general, $\kappa_{\text{total}} = \kappa_e + \kappa_{\text{ph}}$ consists of the electronic charge carrier part κ_e and the phonon term κ_{ph} . The κ_e part can be estimated from the Wiedemann-Franz law $\kappa_e/T = L_0/\rho$, where

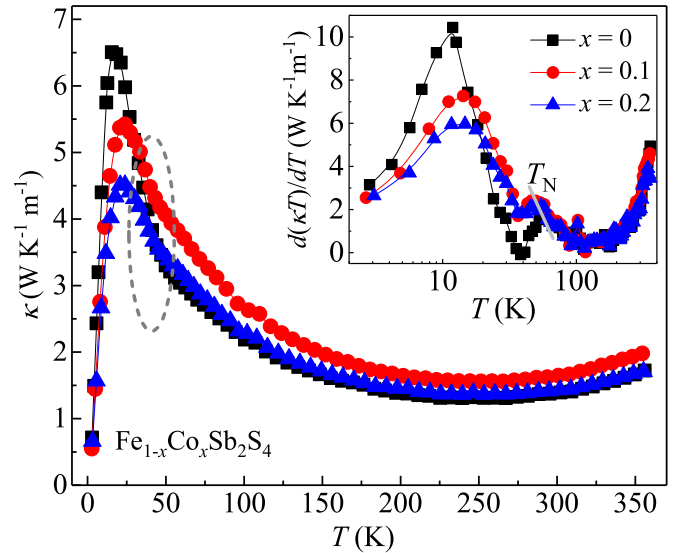


FIG. 5. Temperature-dependent thermal conductivity $\kappa(T)$ of $\text{Fe}_{1-x}\text{Co}_x\text{Sb}_2\text{S}_4$ ($x = 0, 0.1, \text{ and } 0.2$). Inset: $d(\kappa T)/dT$ vs T curves. The solid line is guide to the eye.

$L_0 = 2.45 \times 10^{-8} \text{ W } \Omega \text{ K}^{-2}$ and ρ is the measured electrical resistivity. The estimated κ_e is less than 0.01% of κ_{total} because of the large electrical resistivity of $\text{Fe}_{1-x}\text{Co}_x\text{Sb}_2\text{S}_4$ ($x = 0, 0.1, \text{ and } 0.2$), indicating a predominantly phonon contribution. At room temperature, the $\kappa(T)$ shows relatively low values of $1.39\text{--}1.64 \text{ W K}^{-1} \text{ m}^{-1}$, which could be contributed to the combination of low crystal symmetry and complex structure and chemical composition with heavy element Sb. Moreover, the $\kappa(T)$ shows weak temperature dependence above 150 K. With decreasing temperature, the observed increase in $\kappa(T)$ is consistent with a gradual freezing of phonon umklapp processes, and a typical phonon peak was observed around 20 K. With Co doping, the phonon peak of $x = 0$ is about $6.5 \text{ W K}^{-1} \text{ m}^{-1}$ and it is suppressed significantly to 5.4 and $4.5 \text{ W K}^{-1} \text{ m}^{-1}$ for $x = 0.1$ and 0.2 , respectively. The suppression of $\kappa(T)$ should reflect enhanced phonon scattering, which is, in general, realized by grain boundary, point defects, carrier-phonon scattering, and phonon umklapp scattering [41–43]. The carrier concentrations in our samples are very low and the boundary scattering and umklapp process should not vary significantly by replacing a small amount of Fe with Co. Therefore, the suppression of $\kappa(T)$ should be mostly contributed by the Fe/Co doping disorder-enhanced point-defects scattering. Most importantly, a notable hump feature was observed in the $\kappa(T)$ curves in addition to the phonon peaks. As shown in the inset of Fig. 5, the $d(\kappa T)/dT$ vs T curves exhibit weak kinks around 50 K, of which the temperature slightly decreases with Co doping level x . The hump of $\kappa(T)$ is in good agreement with the observed magnetic transitions, indicating strong spin-lattice coupling in $\text{Fe}_{1-x}\text{Co}_x\text{Sb}_2\text{S}_4$.

The specific heat $C_p(T)$ of $\text{Fe}_{1-x}\text{Co}_x\text{Sb}_2\text{S}_4$ ($x = 0, 0.1, \text{ and } 0.2$) (Fig. 6) approaches the value of 3NR at room temperature, where N is the atomic number in the chemical formula ($N = 7$) and R is the gas constant ($R = 8.314 \text{ J mol}^{-1} \text{ K}^{-1}$), consistent with the Dulong-Petit law. By neglecting the magnon contribution at low temperatures, the specific heat can be

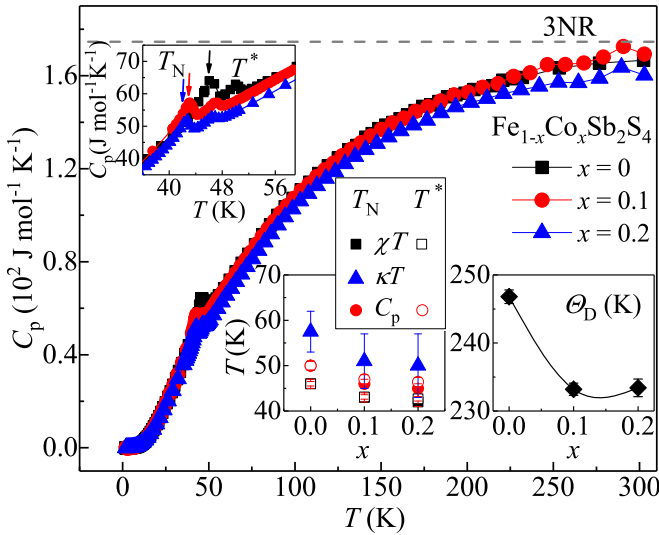


FIG. 6. Temperature-dependent heat capacity of $\text{Fe}_{1-x}\text{Co}_x\text{Sb}_2\text{S}_4$ ($x = 0, 0.1$, and 0.2). Insets: The enlargement of the specific-heat anomaly between 36 K and 60 K, and the evolution of transition temperatures (T_N and T^*) and Debye temperature (Θ_D) as a function of Co content x .

separated into the electronic and phonon parts, $C_p(T) = \gamma T + \beta T^3$. By fitting the $C_p(T)$ data below $T = 6$ K, the obtained Sommerfeld electronic specific-heat coefficient γ is less than $0.005 \text{ J mol}^{-1} \text{ K}^{-2}$, in line with its insulating ground state. For FeSb_2S_4 ($x = 0$), the derived Debye temperature $\Theta_D = 247(1) \text{ K}$ from $\beta = 0.90(1) \text{ mJ mol}^{-1} \text{ K}^{-4}$ using the equation $\Theta_D = [12\pi^4 N R / (5\beta)]^{1/3}$ slightly decreases to $233(1) \text{ K}$ for $x = 0.2$. The enlargement of the specific-heat anomaly between 36 K and 60 K shows an obvious λ -type peak at $T_N = 46.0(5) \text{ K}$ for $x = 0$, corresponding to the formation of long-range AFM ordering, as well as an additional small peak at $T^* = 50(1) \text{ K}$, in good agreement with the magnetic transition observed in the susceptibility curve. This could indicate the subtle magnetostructural effects at the AFM transition, similar to Fe_{1+y}Te , calling for re-examination of the low-temperature structure of FeSb_2S_4 [44]. The evolution of T_N and T^* with x from different methods is finally summarized in the inset of Fig. 6.

To give a better description of the experimental data, we also calculated the band structure of a simple nonmagnetic FeSb_2S_4 using experimental lattice parameters. First-principles calculations based on density-functional theory demonstrate the dominance of Fe $3d$ states near the Fermi level and in partial density of states, as shown in Fig. 7. It is of interest to note that the experimental lattice parameters result in a metallic ground state within our theoretical framework. Since the standard GGA functional tends to underestimate band gaps of semiconductors, the modified Becke-John (mBJ) exchange potential was also utilized to verify the bulk band gap [45]. However, the metallic ground state is robust even in the mBJ exchange potential. An indirect energy gap $\Delta = 158 \text{ meV}$ opens up [Fig. 7(d)] only with fully relaxed structure where $a = 11.274 \text{ \AA}$, $b = 3.636 \text{ \AA}$, $c = 13.821 \text{ \AA}$, which are smaller than

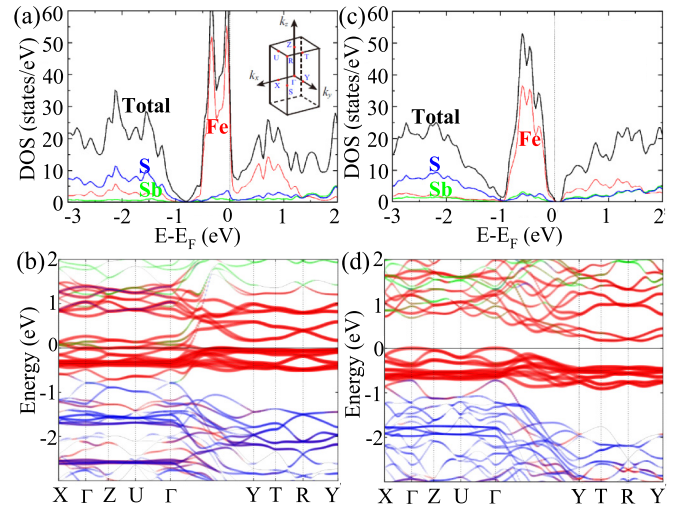


FIG. 7. Density of states and band structure of FeSb_2S_4 using experimental values (a), (b) and DFT-relaxed lattice parameters (c), (d). The states with Fe d , S p , and Sb p character are denoted by thick red, medium blue, and thin green lines, respectively. Inset in (a) shows the sketch of the FeSb_2S_4 Brillouin zone.

the experimental values [$a = 11.385(2) \text{ \AA}$, $b = 3.765(2) \text{ \AA}$, $c = 14.147(2) \text{ \AA}$]. This suggests that insight into the low-temperature crystal and magnetic structure is of interest.

IV. CONCLUSIONS

Our paper has demonstrated the polaronic nature of electronic transport in the magnetic semiconductor alloys $\text{Fe}_{1-x}\text{Co}_x\text{Sb}_2\text{S}_4$ ($x = 0, 0.1$, and 0.2), based on the large discrepancy between activation energy for conductivity E_ρ ($146 \sim 270 \text{ meV}$) and for thermopower E_S ($47 \sim 108 \text{ meV}$). Bulk magnetization and heat capacity of FeSb_2S_4 exhibit two-step magnetic transitions with possible canted AFM ground state. The transition temperatures (T_N and T^*) slightly decrease with increase Co doping level x . The magnetic transitions are also observed in the thermal conductivity measurement, demonstrating not only strong spin-lattice coupling but also thermal conductivity values much smaller from the values found in iron diantimonide. Even though the thermopower S of FeSb_2S_4 is smaller when compared to FeSb_2 , $\text{Fe}_{1-x}\text{Co}_x\text{Sb}_2\text{S}_4$ shows increase of thermopower with x . Given the similarity of its crystal structure to marcasites such as FeSb_2 but also a ternary chemical formula that offers additional tunability when compared to it, further anion substitutions might enhance its thermoelectric performance.

ACKNOWLEDGMENT

This work was supported by the U.S. Department of Energy (DOE), Office of Science, Basic Energy Sciences as a part of the Computational Materials Science Program (materials synthesis and characterization). X-ray studies benefited from using the 8-ID (ISS) beamline of the National Synchrotron Light Source II, a U.S. DOE Office of Science User Facility operated for the DOE Office of Science by Brookhaven National Laboratory under Contract No. DE-SC0012704.

- [1] C. Petrovic, J. W. Kim, S. L. Bud'ko, A. I. Goldman, P. C. Canfield, W. Choe, and G. J. Miller, *Phys. Rev. B* **67**, 155205 (2003).
- [2] C. Petrovic, Y. Lee, T. Vogt, N. Dj. Lazarov, S. L. Budko, and P. C. Canfield, *Phys. Rev. B* **72**, 045103 (2005).
- [3] R. Hu, K. Wang, H. Ryu, H. Lei, E. S. Choi, M. Uhlarz, J. Wosnitza, and C. Petrovic, *Phys. Rev. Lett.* **109**, 256401 (2012).
- [4] A. Bentien, S. Johnsen, G. K. H. Madsen, B. B. Iversen, and F. Steglich, *Europhys. Lett.* **80**, 17008 (2007).
- [5] Q. Jie, R. Hu, E. Bozin, A. Llobet, I. Zaliznyak, C. Petrovic, and Q. Li, *Phys. Rev. B* **86**, 115121 (2012).
- [6] H. Takahashi, R. Okazaki, S. Ishiwata, H. Taniguchi, A. Okutani, M. Hagiwara, and I. Terasaki, *Nat. Commun.* **7**, 12732 (2016).
- [7] C. Tian, C. Lee, E. Kan, F. Wu, and M. H. Whangbo, *Inorg. Chem.* **49**, 10956 (2010).
- [8] P. Léone, C. D. Brochard, G. André, and Y. Moëlo, *Phys. Chem. Miner.* **35**, 201 (2008).
- [9] S. F. Matar, R. Wehrich, D. Kurowsky, A. Pfitzner, and V. Eyert, *Phys. Rev. B* **71**, 235207 (2005).
- [10] A. Pfitzner and D. Kurowski, *Z. Kristallogr.* **215**, 373 (2000).
- [11] H. Djieutedjeu, J. P. A. Makongo, A. Rotaru, A. Palasyuk, N. J. Takas, X. Y. Zhou, K. G. S. Ranmohotti, L. Spinu, C. Uher, and P. F. P. Poudeu, *Eur. J. Inorg. Chem.* **2011**, 3969 (2011).
- [12] H. Djieutedjeu, X. Y. Zhou, H. Chi, N. Haldolaarachchige, K. G. S. Ranmohotti, C. Uher, D. Young, and P. F. P. Poudeu, *J. Mater. Chem. C* **2**, 6199 (2014).
- [13] S. M. Li, H. Z. Zhao, H. Zhang, G. K. Ren, N. Liu, D. D. Li, C. S. Yang, S. F. Jin, D. S. Shang, W. H. Wang, Y. H. Lin, L. Gu, and X. L. Chen, *RSC Adv.* **5**, 99065 (2015).
- [14] S. Lee, E. Fischer, J. Czerniak, and N. Nagasundaram, *J. Alloys Compd.* **197**, 1 (1993).
- [15] K. G. S. Ranmohotti, H. Djieutedjeu, and P. F. P. Poudeu, *J. Am. Chem. Soc.* **134**, 14033 (2012).
- [16] K. Łukaszewicz, A. Pietraszko, J. S. Damm, A. Kajokas, J. Grigas, and H. Drulis, *J. Solid State Chem.* **162**, 79 (2001).
- [17] M. Wintenberger and G. André, *Physica B* **162**, 5 (1990).
- [18] P. Bonville, C. Garcin, A. Gérard, P. Imbert, and M. Wintenberger, *Hyperfine Interact.* **52**, 279 (1989).
- [19] B. Periotto, T. B. Žunić, and F. Nestola, *Can. Mineral.* **50**, 201 (2012).
- [20] H. Djieutedjeu, P. F. P. Poudeu, N. J. Takas, J. P. A. Makongo, A. Rotaru, K. G. S. Ranmohotti, C. J. Anglin, L. Spinu, and J. B. Wiley, *Angew. Chem., Int. Ed.* **49**, 9977 (2010).
- [21] K. G. S. Ranmohotti, H. Djieutedjeu, J. Lopez, A. Page, N. Haldolaarachchige, H. Chi, P. Sahoo, C. Uher, D. Young, and P. F. P. Poudeu, *J. Am. Chem. Soc.* **137**, 691 (2015).
- [22] F. Hulliger, *Nature (London)* **198**, 1081 (1963).
- [23] F. Hulliger, *Struct. Bond. (Berlin)* **4**, 83 (1967).
- [24] J. B. Goodenough, *J. Solid State Chem.* **5**, 144 (1972).
- [25] L. Bindi and S. Menchetti, *Miner. Petrol.* **85**, 131 (2005).
- [26] V. A. Gasyimov, G. N. Gasyimova, and O. M. Aliev, *Inorg. Mater.* **40**, 1095 (2004).
- [27] R. Hu, V. F. Mitrovic, and C. Petrovic, *Phys. Rev. B* **74**, 195130 (2006).
- [28] R. Hu, V. F. Mitrovic, and C. Petrovic, *Phys. Rev. B* **76**, 115105 (2007).
- [29] M. Weinert, E. Wimmer, and A. J. Freeman, *Phys. Rev. B* **26**, 4571 (1982).
- [30] P. Blaha, K. Schwartz, G. K. H. Madsen, D. Kvasnicka, and J. Luitz, *WIEN2K, An Augmented Plane Wave and Local Orbitals Program for Calculating Crystal Properties* (Techn. Universität Wien, Austria, 2001).
- [31] J. P. Perdew, K. Burke, and M. Ernzerhof, *Phys. Rev. Lett.* **77**, 3865 (1996).
- [32] M. J. Buerger and T. Hahn, *Am. Mineral.* **40**, 226 (1955).
- [33] *X-Ray Absorption: Principles, Applications, Techniques of EXAFS, SEXAFS, XANES*, edited by R. Prins and D. C. Koningsberger (Wiley, New York, 1988).
- [34] I. G. Austin and N. F. Mott, *Adv. Phys.* **50**, 757 (2001).
- [35] J. B. Goodenough, *Magnetism and Chemical Bond* (Wiley Intersciences, London, 1963).
- [36] J. E. Greedan, *J. Mater. Chem.* **11**, 37 (2001).
- [37] D. Dai and M.-H. Whangbo, *J. Chem. Phys.* **121**, 672 (2004).
- [38] R. W. Hu, E. S. Bozin, J. B. Warren, and C. Petrovic, *Phys. Rev. B* **80**, 214514 (2009).
- [39] C. D. Brochard, P. Léone, G. André, and Y. Moëlo, *Mater. Res. Bull.* **44**, 759 (2009).
- [40] W. Bao, Y. Qiu, Q. Huang, M. A. Green, P. Zajdel, M. R. Fitzsimmons, M. Zhernenkov, S. Chang, M. Fang, B. Qian, E. K. Vehstedt, J. Yang, H. M. Pham, L. Spinu, and Z. Q. Mao, *Phys. Rev. Lett.* **102**, 247001 (2009).
- [41] G. S. Nolas and H. J. Goldsmid, *Thermal Conductivity: Theory, Properties and Application* (Kluwer Academic, New York, 2004).
- [42] J. Callaway, *Phys. Rev.* **113**, 1046 (1959).
- [43] G. A. Glassbrenner and G. A. Slack, *Phys. Rev.* **134**, A1058 (1964).
- [44] I. A. Zaliznyak, Z. J. Xu, J. M. Tranquada, G. D. Gu, V. Solovyev, V. N. Glazkov, A. I. Zheludev, V. O. Garlea, and M. B. Stone, *Phys. Rev. B* **85**, 085105 (2012).
- [45] F. Tran and P. Blaha, *Phys. Rev. Lett.* **102**, 226401 (2009).

Correction: Some statements in the Acknowledgment section have been updated.